Noname manuscript No.
(will be inserted by the editor)

Turbulence generated by an array of opposed piston-driven synthetic jet actuators

Kohei Yamamoto · Tomoaki Watanabe · Koji Nagata

Received: 1 June 2021 / Received: 4 October 2021 / Accepted: 4 November 2021

Abstract This paper investigates turbulence generated by an array of opposed piston-driven synthetic jet actuators in a closed chamber. Each actuator intermittently generates supersonic jets with four orifice holes, and the interaction of 32 supersonic jets produces turbulence. Velocity measurement is conducted with particle image velocimetry using oil mist as the tracer particles, which are internally generated by the synthetic jet actuators. The turbulence with a small mean velocity is generated at the central region of the chamber, where the root-mean-square (rms) velocity fluctuations are also almost uniform in space. The rms velocity fluctuations around the chamber center are about 1.2 times larger in the jet direction than in other directions. The strongly intermittent nature of supersonic synthetic jets causes large-scale intermittency of turbulence. The turbulent Reynolds number and turbulent Mach number reach $O(10^3)$ and $O(10^{-2})$, respectively, at the chamber center. Although the turbulent Mach number at the chamber center is not large, the generation process of turbulence due to the supersonic jets is strongly influenced by compressibility. Therefore, density variations exist in turbulence, where the shadowgraph image exhibits the brightness distribution with a characteristic length scale related to the Kolmogorov scale. The shape of longitudinal velocity autocorrelation functions and the relation between the turbulent Reynolds number

Kohei Yamamoto · Tomoaki Watanabe · Koji Nagata
Department of Aerospace Engineering, Nagoya University, Nagoya 464-8603, Japan
Tel.: +81-52-789-3279
E-mail: watanabe.tomoaki@c.nagoya-u.jp

and velocity derivative flatness agree well with previous studies on incompressible turbulence.

Keywords Synthetic jets · Compressible turbulence · Supersonic jets

1 Introduction

Turbulence is an important phenomenon in physics and engineering problems (Davidson, 2004). Laboratory experiments play an important role in testing the theories and models of turbulence. Because of the complexity of turbulence, several assumptions are often made in theoretical researches, e.g., stationarity, homogeneity, and isotropy for statistics and incompressibility. Therefore, various methods have been proposed to generate turbulence with desired properties in laboratory experiments. Wind tunnels are widely used in laboratory experiments of turbulence. Nearly homogeneous isotropic turbulence can be generated by a grid installed in a uniform flow in wind tunnels (e.g., Comte-Bellot and Corrsin 1966; Uberoi and Wallis 1967; Mydlarski and Warhaft 1996; Kang et al. 2003; Krogstad and Davidson 2010; Valente and Vassilicos 2011; Kitamura et al. 2014; Djenidi et al. 2015). Grid turbulence has been studied for many years to investigate decaying, homogeneous isotropic turbulence. A multi-fan wind tunnel is also used to generate decaying, homogeneous isotropic turbulence in the wind tunnel by the interaction of flows induced by a large number of fans (Ozono and Ikeda, 2018; Takamure and Ozono, 2019).

Stirring devices in a closed chamber have also been used by many researchers for experimental studies on turbulence. Birouk et al. (2003) used eight electrical fans connected to a chamber with a spherical interior and reported that nearly homogeneous isotropic turbulence was generated near the chamber center. Turbulence generation with multiple fans was also reported by other reserchers (Semenov, 1965; Zimmermann et al., 2010; Ravi et al., 2013; Xu et al., 2017; Bradley et al., 2019). Similar facilities that generate turbulence in a closed chamber were developed with synthetic jets. Hwang and Eaton (2004) used eight synthetic jet actuators connected on the corners of a cubic chamber to produce homogeneous isotropic turbulence. A similar facility with synthetic jet actuators was also developed by Goepfert et al. (2010). Furthermore, Variano et al. (2004) used an array of synthetic jets to generate nearly homogeneous isotropic turbulence in a water tank. It was also shown that nearly homogeneous isotropic turbulence can be generated by randomly actuated jets (Bellani and Variano, 2014; Carter et al., 2016; Pérez-Alvarado et al., 2016). On the other hand, Krawczynski et al. (2010) generated axisymmetric turbulence with opposed continuous round jets. Instead of installing a turbulence-generating grid in wind tunnels, the grid can be oscillated in a water tank to generate turbulence with a small mean velocity. Experiments of oscillating-grid turbulence are often conducted to investigate the mixing across density interfaces (Thompson and Turner, 1975; Hopfinger and Toly, 1976; De Silva and Fernando, 1994). Another method of generating turbulence

with a grid is to move the grid in a water tank. Stably stratified turbulence is often investigated with the towing-grid experiments (Yap and Van Atta, 1993; Fincham et al., 1996; Praud et al., 2005; Xiang et al., 2015).

These turbulence chambers that generate turbulent flows with a small mean velocity in a closed space have been used for a wide range of problems associated with turbulence. A Lagrangian investigation was conducted for the evaporation rate of diethyl ether droplets in the turbulence generated by synthetic jets (Marié et al., 2017). Turbulence beneath an air-water interface was investigated with an array of synthetic jets (Variano and Cowen, 2008). Hwang and Eaton (2006) used the sealed chamber equipped with synthetic jet actuators to investigate the particle dispersion in turbulence. These studies prove that turbulence in a closed chamber is useful for experimental investigation on a wide range of problems related to turbulence. The above examples of turbulence chambers are limited to a low Mach number regime, which can be treated as incompressible flows. Experiments of compressible turbulence are often conducted for boundary-free inhomogeneous flows, such as supersonic jets (Wernet, 2016), wakes (Bonnet et al., 1984), and mixing layers (Clemens and Mungal, 1995). Experiments of grid turbulence have also been reported in previous studies with shock tube facilities and supersonic or transonic wind tunnels. These studies often investigated the interaction between a shock wave and grid turbulence (Keller and Merzkirch, 1990; Honkan and Andreopoulos, 1992; Agui et al., 2005; Tamba et al., 2019), while some experiments focused on compressible turbulence generated by a grid (Zwart et al., 1997; Briassulis et al., 2001). Measurements of reliable statistics of turbulence are often difficult in shock tubes because a uniform flow in the shock tube is sustained only for a short time interval.

Hot-wire anemometry is widely used for velocity measurement in incompressible turbulent flows. However, a complicated calibration process of the hot-wire anemometry is required for compressible flows because of temperature and density variations. Furthermore, a hot-wire anemometer used for compressible flows provides mass flux, which has to be decoupled to obtain velocity with several assumptions (Kovasznay, 1950). Therefore, laser Doppler velocimetry and particle image velocimetry (PIV) are expected to play important roles in the velocity measurement of compressible turbulence. It should be noted that PIV measurement of compressible turbulence can be more easily conducted for turbulence chambers with a small mean velocity than high-speed wind tunnels. Compressible turbulence is often characterized by a turbulent Mach number $M_T = \sqrt{3}u_{rms}/a$ defined with root-mean-squared (rms) velocity fluctuations u_{rms} and the speed of sound a calculated with a mean temperature T. In fully developed grid turbulence with a mean velocity U_0, turbulence intensity u_{rms}/U_0 is smaller than 0.1 (Uberoi and Wallis, 1967). For example, if turbulence of air has $u_{rms}/U_0 = 0.05$, $M_T = 0.1$, and $T = 300$ [K], the maximum instantaneous velocity reaches about $U_0 + 3u_{rms} \approx 460$ m/s. Here, $3u_{rms}$ is used for the estimation because fluctuations greater than $3u_{rms}$ hardly occur when the probability density function is given by a Gaussian function. As the investigation of turbulence also requires high spatial resolution, PIV

measurements of turbulence with such a large velocity are not easy and require very short frame-straddling time (Scarano and Van Oudheusden, 2003). For the same turbulent Mach number and temperature, the instantaneous velocity in turbulence with zero mean velocity reaches about $3u_{rms} \approx 60$ m/s. Therefore, it is expected that turbulence chambers are also useful for studying various phenomena associated with compressible turbulence in laboratory experiments.

Compressible turbulence facilities with a small mean velocity have hardly been discussed in the existing literature even though such facilities have been used for incompressible turbulence. The present study extends the turbulence generation with multiple synthetic jets considered in previous studies to a high-speed flow regime. We develop a turbulence chamber with high-speed synthetic jet actuators, each of which consists of a cylinder with an orifice plate at the top and a piston actuator driven by a DC motor. This piston-driven synthetic jet actuator can produce a flow with a larger velocity than conventional synthetic jet actuators with piezoelectrically driven diaphragms (Crittenden and Glezer, 2006; Gilarranz et al., 2005; Traub et al., 2012; Sakakibara et al., 2018). The maximum velocity of the piston-driven synthetic jet can be supersonic when the actuator is operated at high frequency. The facility developed in this study uses eight piston-driven synthetic jet actuators installed on two opposed faces of a rectangular box, in which turbulence is generated by the interaction of the high-speed synthetic jets. We characterize the generated turbulence with PIV and shadowgraph visualization.

The paper is organized as follows. The turbulence chamber developed in this study is described in Sec. 2 while the measurement methods are described in Sec. 3. Section 4 presents the results of PIV measurement, temperature measurement, and shadowgraph visualization. Finally, the paper is summarized in Sec. 5.

2 Turbulence generation by an array of opposed piston-driven synthetic jet actuators

2.1 Piston-driven syntethic jet actuator

The turbulence chamber developed in this study utilizes piston-driven synthetic jet actuators, whose characteristics were investigated in our previous paper (Sakakibara et al., 2018). Each actuator consists of a four-stroke model engine (O.S. Engine, FSα-56) and a DC brushless motor (Cobra, C-2826/10). The engine shaft is connected to the motor via an Oldham coupling. The motor is controlled by an electronic speed controller (Cobra, 40A ESC w/6A Switching BEC) with pulse width modulation signals from a microcontroller (Arduino). The motor and the electronic speed controller are powered by a 12V-50A switched-mode power supply (Cosel, PLA600F-12). An aluminum orifice plate with four round holes is installed on the top of the cylinder after the original cylinder top of the engine is removed. The piston movement by the

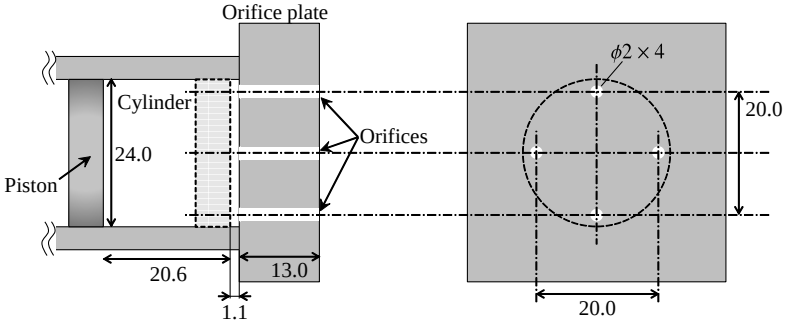

Fig. 1 Piston synthetic jet actuator with four orifice holes. All dimensions are in mm.

motor produces synthetic jets with orifice holes. Figure 1 shows a schematic diagram of the actuator. The inner diameter and volume of the cylinder are 24.0 mm and 9.8 cc, respectively. The piston has a stroke length of 20.6 mm, for which the displacement volume is 9.3 cc. The top of the cylinder has four orifice holes with a diameter of 2 mm. The actuation frequency f, defined with a rotational speed of the motor, can be measured by a magnetic sensor with a magnet attached to the engine shaft. The present paper reports the experiments conducted at $f = 150$ Hz.

Sakakibara et al. (2018) investigated the flow induced by the piston-driven synthetic jet actuator with the four orifice holes at $f = 150$ Hz. The pressure in the cylinder was measured by a piezoresistive pressure transducer (Endevco, 8510B-200), which was mounted on the orifice plate with an additional hole on the plate. The pressure history over a cycle indicated that the velocity through the orifice holes is subsonic in a suction phase. It was also shown that the supersonic jets with the maximum jet Mach number of 1.2 are ejected from the orifice holes in a blowing phase.

2.2 Turbulence generation by opposed piston-driven syntetic jets

We develop a turbulence chamber in which opposed piston-driven synthetic jet actuators generate turbulence in a box. Figure 2(a) illustrates a schematic diagram of the turbulence chamber with the main components of the facility while its picture is shown in Fig. 2(b). Eight piston-driven synthetic jet actuators are placed on two opposite surfaces of the chamber, whose interior is a rectangular parallelepiped. The motors and engines are fixed on aluminum frames, which are placed on rubber cushions. One side of the chamber has four actuators, each of which has four orifice holes with a diameter of 2 mm. Hence, 32 synthetic jets are produced in the chamber. The jet direction is denoted by x while y and z represent the vertical and spanwise directions, respectively. The size of the chamber interior, $(L_x \times L_y \times L_z)$, is $100 \times 100 \times 95$ mm^3. The sidewalls of the chamber are optical glass plates with 5 mm thickness, while

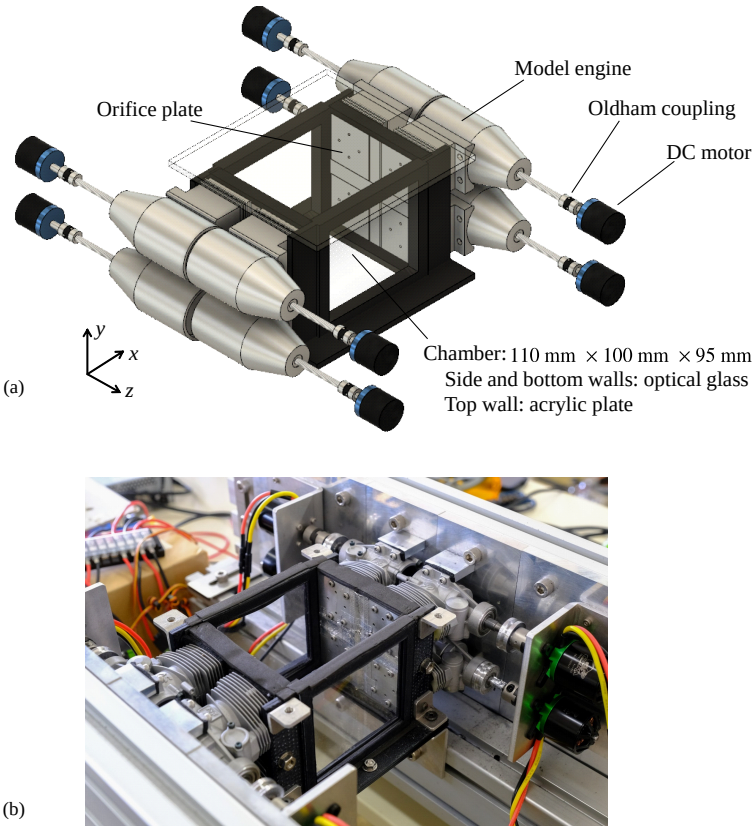

Fig. 2 (a) Schematic diagram of the turbulence chamber developed with piston-driven synthetic jet actuators. (b) A photo of the turbulence chamber.

the bottom wall is an optical glass plate with 3 mm thickness. These glasses are held with flanges manufactured by a fused filament fabrication 3D printer. The top wall of the chamber is an acrylic plate. The gap between the chamber walls and the side of the orifice plates is filled with a foam rubber sheet.

Figure 3 shows the layout of the actuators on one side of the chamber. The space of 10 mm between the orifice plates is covered by aluminum tape. This spacing is due to the size of the engines under the orifice plates. The nearest holes of the two plates are separated by 32 mm while the distance between the centers of the plates is 52 mm. The distance between the actuators on the opposite planes is 100 mm.

The experiments are conducted with the actuation frequency of $f = 150$ Hz, for which the characteristics of the supersonic synthetic jet were investigated in Sakakibara et al. (2018). The initial piston phases of the eight actuators are not matched. The fluctuations in the actuation frequency are about ± 3 Hz. At the beginning of the experiments, the synthetic jet actuator is operated un-

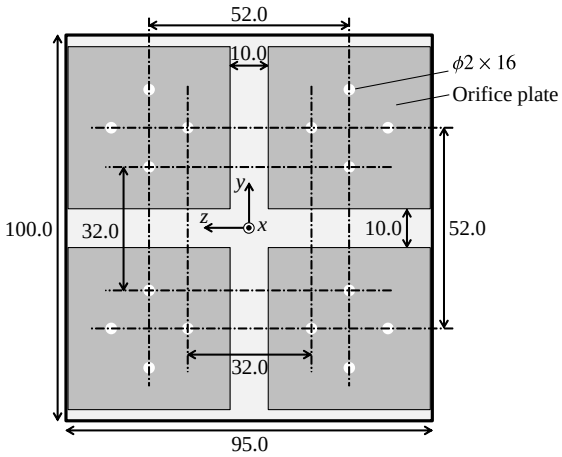

Fig. 3 Alignments of orifice holes on one side of the chamber. A thick line represents the sidewalls of the chamber. The size of the holes in the figure is larger than the actual size for visibility. All dimensions are in mm.

der a transitional state, for which the frequency depends on the initial phase and can be different from 150 Hz. Therefore, the present experiments cannot control the phase difference among eight synthetic jet actuators. The experiments are repeated with different initial phases, and ensemble averages are used to evaluate the statistics. It will be shown in Sec. 4 that the mean velocity and rms velocity fluctuations are similar in two independent experiments conducted with different initial phases. The actuation frequency is high enough to generate the supersonic jets. The PIV measurement uses the oil mist generated by high temperature in the cylinder, which is caused by the fluid compression by the piston, as explained in the next section. The temperature in the cylinder does not become sufficiently high for the tracer particle generation if the experiments are conducted with lower f.

It should be noted that the experimental conditions can be varied by changing the nozzle shape, e.g., a divergent-convergent nozzle, even if f is fixed at 150 Hz. This feature may be useful for investigating the universality of turbulence generated under different conditions. However, the present study only considers a simple sharp-edged orifice because the synthetic jet generated with the orifice was investigated in detail in previous papers (Crittenden and Glezer, 2006; Sakakibara et al., 2018).

3 Measurements

3.1 Particle image velocimetry

The PIV is used to measure two components of velocity vectors on x-y planes. The PIV system consists of a double-pulse Nd:YAG laser (Dantec Dynamics, Dual Power 65-15) and a high-speed camera (Dantec Dynamics, SpeedSense 9070), which is equipped with a camera lens with a focal length of 60 mm (Nikkon, Ai AF Micro-Nikkor 60 mm f/2.8D). The laser and camera are controlled with a synchronizer and PIV software (Dantec Dynamic Studio). A laser light sheet with a thickness of 1 mm is produced by light sheet optics mounted on the laser. The laser illuminates a x-y plane from the bottom of the chamber while the camera facing in the z direction takes images through the glass window. The time interval of two laser pulses is 2.5 μs while each pulse has a width less than 4 ns and the maximum pulse energy of 400 mJ. The camera records pairs of particle images, and each pair is analyzed with an adaptive PIV algorithm implemented in Dantec Dynamic Studio. An interrogation window size is 32×32 pixels.

The PIV measurement is conducted on the x-y planes at $z = 0$ and 26 mm, which are referred to as a midplane and a jet plane, respectively. $z = 0$ mm is the chamber center while four orifice holes are located at $z = 26$ mm as shown in Fig. 3. The velocity vectors are measured in an area of 66×54 mm^2 centered at $(x, y) = (0, 0)$ with a spacing of 0.7 mm in both x and y directions. The PIV measurement is started 5 s after all the actuators are turned on. During 5 s, the jets are ejected 750 times, which can be considered enough for the turbulence to be a statistically steady state. In each experiment, 300 image pairs are acquired over 20 s at a sampling rate of 15 Hz. The measurement is repeated 4 times and 1,200 image pairs are acquired. The integral time scale, defined as the integral length scale divided by root-mean-squared velocity fluctuations, is of the order of 10^{-3} s, which is much shorter than the time interval of the two consecutive image pairs for the PIV, $1/15 \approx 0.067$ s. Therefore, 1,200 independent samples of the velocity vectors are obtained by the PIV measurement.

Before the experiments are conducted, a small amount (about 1 ml) of 10W-30 engine oil for 4-cycle engines (Sanyu Kagaku, 4 cycle motor oil) is put on the internal surface of the cylinders for lubrication. This oil is vaporized when the temperature exceeds about 420 K. The compression of fluid by the piston significantly increases the temperature in the cylinder of piston-driven synthetic jet actuators as shown by a quasi-static simulation model (Crittenden and Glezer, 2006), which implies that the temperature exceeds 420 K during the cycle (Sakakibara et al., 2018). The oil is evaporated in the cylinder because of the high temperature. The hot fluid with the oil vapor is ejected into the chamber, where the temperature is lower than in the cylinder. Then, the temperature of the jet fluid decreases in the chamber, and oil mist is generated by condensation. The oil mist is used as the tracer particles of PIV. The particle generation process in the piston-driven synthetic jet actuators is the same as the typical fog generators used for PIV, in which fog liquid is

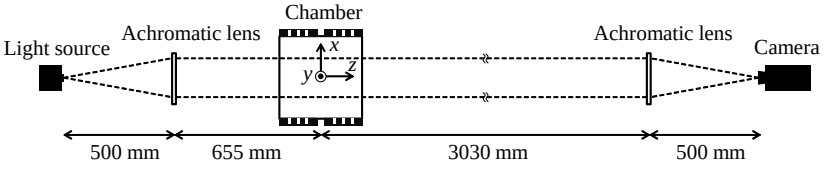

Fig. 4 The schematic of the optical system for shadowgraph visualization.

vaporized with a heat exchanger and condensed when the vaporized liquid is mixed with cool ambient air. The engine oil used in this study mainly consists of mineral oil, which is widely used to generate tracer particles for PIV and flow visualization (Williams et al., 2015; Klewicki and Hirschi, 2004). The condensation of vaporized mineral oil can produce droplets whose diameter is as small as 0.3 μm (Beresh et al., 2015; Wernet, 2007).

3.2 Shadowgraph visualization

Turbulence is visualized with a shadowgraph method. Figure 4 shows the optical system, which consists of two achromatic lenses with a focal length of 500 mm, a point light source (Xenon lamp), and a high-speed camera (Dantec Dynamics, Speed Sense 9072). The light collimated by the achromatic lens passes through the chamber in the z direction. The lens diameter is 46 mm. The camera captures shadowgraph images around the chamber center at a sampling rate of 2,200 Hz.

3.3 Temperature measurement

The work by the pistons increases the fluid temperature in the cylinder. The synthetic jet actuators also input kinetic energy in the chamber, where the kinetic energy dissipation may also increase temperature. Therefore, temperature measurement is also conducted with a K-type thermocouple thermometer (A&D, AD-5601A). The sensor probe (A&D, AD-1214) is inserted in the chamber through a small gap between the chamber top cover and the flange of the side window. The probe is fixed to measure temperature at the chamber center. The frequency response of the thermocouple thermometer is not enough to capture temperature fluctuations of turbulence, and the measurement provides temperature averaged over a certain time interval. We use the thermocouple thermometer to examine whether or not the mean temperature reaches a steady state.

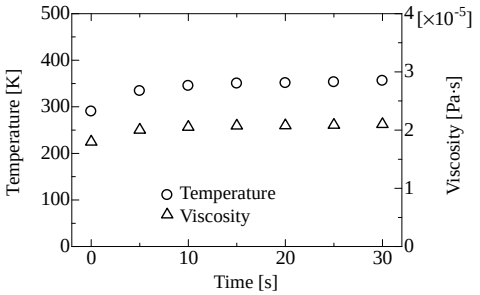

Fig. 5 Temperature and viscosity variations with time after the piston-driven synthetic jet actuators are turned on.

4 Results and discussion

4.1 Temperature variation

The temperature measurement is conducted over 30 s once the synthetic jet actuators are turned on. The output of the thermometer is saved every 5 s. The viscosity coefficient μ is estimated from temperature T by Sutherland's law:

$$\mu = \mu_0 \left(\frac{T}{T_0} \right)^{3/2} \frac{T_0 + S}{T + S} \tag{1}$$

with $\mu_0 = 1.742 \times 10^{-5}$ [Pa s], $T_0 = 273$ [K], and $S = 110.4$ [K]. Figure 5 shows the temporal variations of T and μ. The temperature increases with time from 290 K to 350 K. The thermocouple thermometer is not able to accurately measure the initial temperature increase because the frequency response is not sufficient, and it is expected that the temperature increases faster. The temperature in the chamber reaches a steady state of 350 K. Therefore, $\mu = 2.08 \times 10^{-5}$ [Pa s] also hardly varies with time after 5 s. In the rest of the paper, we use $T = 350$ [K] and $\mu = 2.08 \times 10^{-5}$ [Pa s] as the reference values of temperature and viscosity at the steady state.

4.2 Velocity statistics

PIV measures velocity components in the x and y directions, which are denoted by $u(x, y)$ and $v(x, y)$. Figure 6 shows the velocity vectors measured on the jet plane and midplane. The jets with velocity of about 100 m/s are observed at $y \approx \pm 16$ mm on the jet plane in Fig. 6(a) because the orifice holes on the jet plane are located at $y = \pm 16$ mm. It should be noted that the jets do not appear in every PIV image because of the intermittent formation of the synthetic jets. The midplane at $z = 0$ does not have orifice holes in Fig. 3. Thus, the velocity vectors in Fig. 6(b) are oriented in various directions without strong influences of the jets in the $\pm x$ directions.

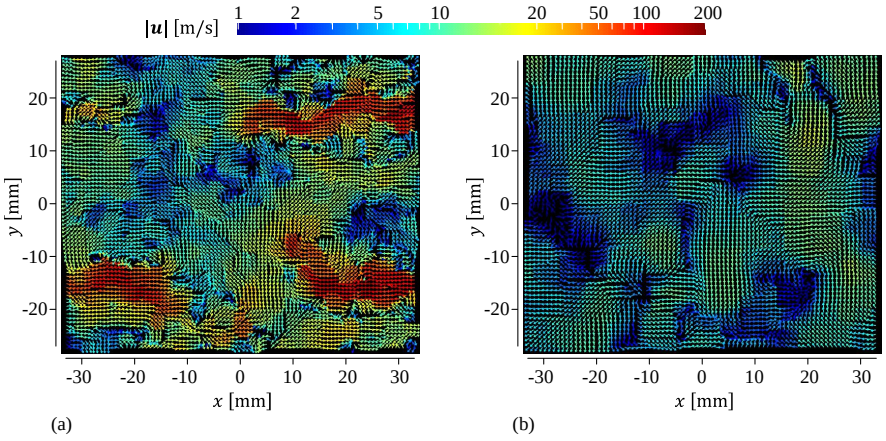

Fig. 6 Velocity vectors on (a) jet plane and (b) midplane. The vectors are colored by the magnitude of velocity vectors $|\mathbf{u}|$, where a logarithmic scale is used for the color.

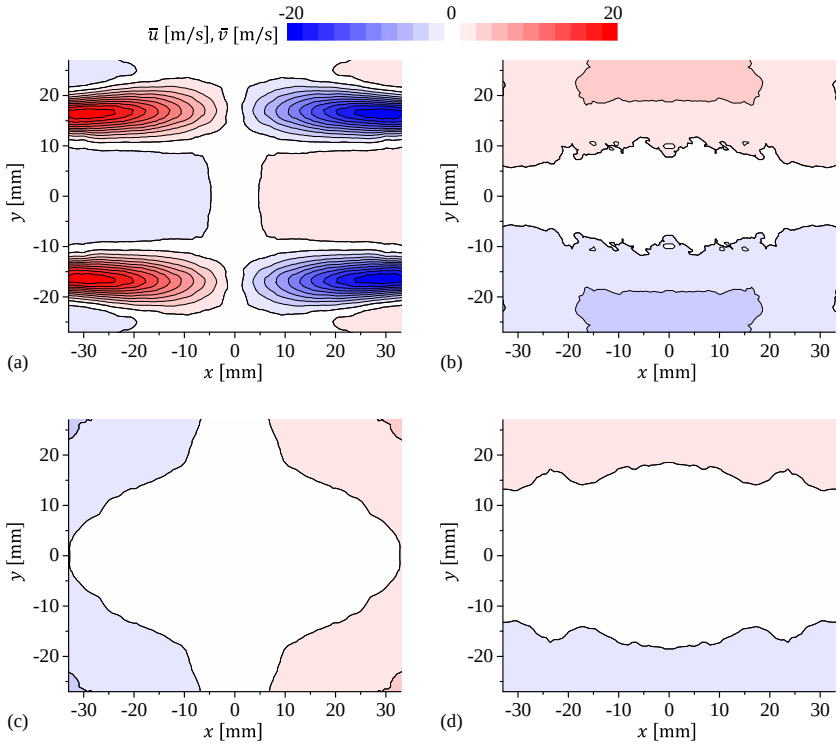

Fig. 7 Mean velocity profiles on (a, b) jet plane and (c, d) midplane: (a, c) $\overline{u}$; (b, d) $\overline{v}$.

Velocity statistics are calculated with an ensemble average defined as

$$\overline{f}(x,y) = \frac{1}{N}\sum_{n=1}^{N} f^{(n)}(x,y), \tag{2}$$

where N is the number of samples and the superscript (n) denotes nth sample. Furthermore, the statistics are symmetric with respect to $(x,y) = (0,0)$, and samples in four quadrants of (x,y) are statistically identical. Therefore, the samples in the four quadrants are used together to improve the statistical convergence. Fluctuations of a variable f are denote by $f'^{(n)}(x,y) = f^{(n)}(x,y) - \overline{f}(x,y)$. Root-mean-squared velocity (rms) fluctuations are defined as $u_{rms} = \sqrt{\overline{u'^2}}$ and $v_{rms} = \sqrt{\overline{v'^2}}$.

Figure 7 shows mean velocity components $\overline{u}$ and $\overline{v}$ on (a, b) the jet plane and (c, d) the midplane. Large positive and negative values of $\overline{u}$ appear at $y = \pm 16$ mm in Fig. 7(a) since the holes are located at these heights. The maximum value of $|\overline{u}|$ is about 20 m/s. Figure 7(b) shows that $\overline{v}$ on the jet plane is not as large as $\overline{u}$ although the mean flows toward the bottom and top are found for $y < -12$ mm and $y > 12$ mm, respectively. Here, $\overline{v}$ on the jet plane is less than 4 m/s. The mean velocity on the midplane is smaller than on the jet plane. The white color in Fig. 7 indicates that $|\overline{u}|$ or $|\overline{v}|$ is smaller than 0.95 m/s. This region with $|\overline{u}| \leq 0.95$ m/s is found for $|x| \lesssim 30$ mm and $|y| \lesssim 15$ mm in Fig. 7(c). $|\overline{v}|$ is also smaller than 0.95 m/s for $|y| \lesssim 15$ in Fig. 7(d). Thus, the mean velocity and its spatial gradient are small around the chamber center.

Figure 8 shows rms velocity fluctuations u_{rms} and v_{rms} on (a, b) the jet plane and (c, d) the midplane. Since the jets are intermittently ejected from the orifices, u_{rms} is large at $y = \pm 16$ mm on the jet plane. The maximum value of u_{rms} is about 40 m/s. u_{rms} and v_{rms} are comparable near the center of the jet plane. On the midplane in Figs. 8(c, d), u_{rms} and v_{rms} weakly depend on x and y. The rms velocity fluctuations are about 5-7 m/s at the chamber center, where the velocity fluctuations are larger than the mean velocity, which is smaller than 1 m/s. Figure 9 complements the information given in the two-dimensional plots of u_{rms} and v_{rms}, by showing the vertical profiles at $x = 0$ and 16 mm on the midplane. The midplane has $u_{rms} \approx$ 6-7 m/s and $v_{rms} \approx$ 5-6 m/s, which weakly depend on x and y around the chamber center. Figure 10 presents u_{rms}/v_{rms} on the midplane. $u_{rms}/v_{rms} =$ 1.2-1.3 for $|x| \lesssim 15$ and $|y| \lesssim 15$, and the rms velocity is larger for the x component. Experiments of grid turbulence also reported that u_{rms} (streamwise velocity) is slightly larger than v_{rms} (transverse velocity) with $u_{rms}/v_{rms} \approx$ 1.1-1.2 (Uberoi and Wallis, 1967; Mydlarski and Warhaft, 1996). Krawczynski et al. (2010) investigated turbulence generated by opposed continuous round jets in a rectangular chamber. They observed that the ratio of rms velocity fluctuations in the jet and transverse directions becomes smaller than 1 because the collision of the opposed jets generates large velocity fluctuations in the transverse directions. However, the formation of the synthetic jets is intermittent, and the

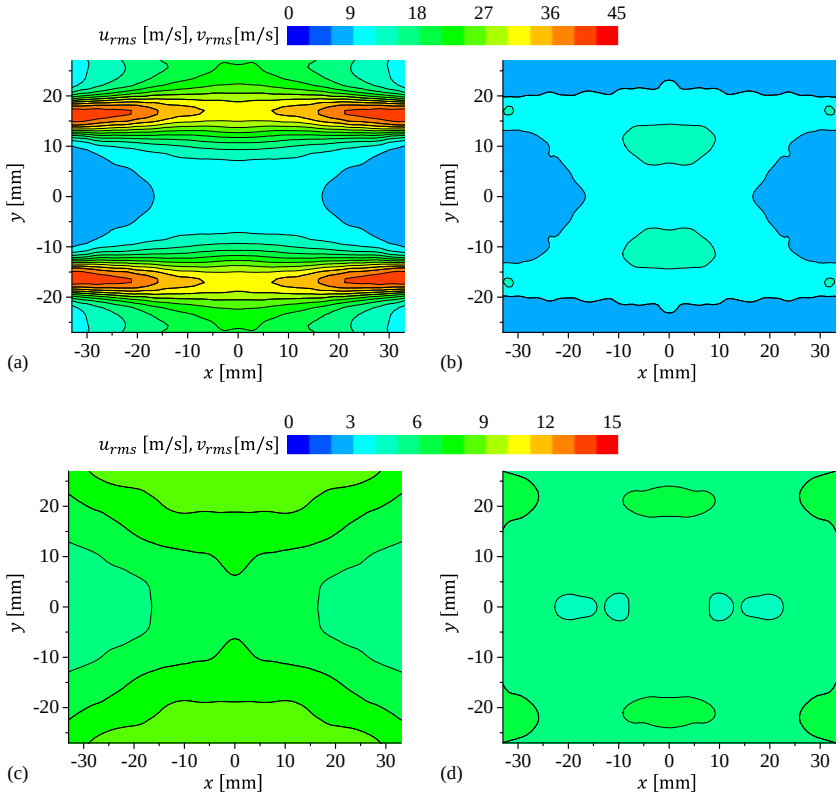

Fig. 8 Rms velocity fluctuations on (a, b) jet plane and (c, d) midplane: (a, c) u_{rms}; (b, d) v_{rms}.

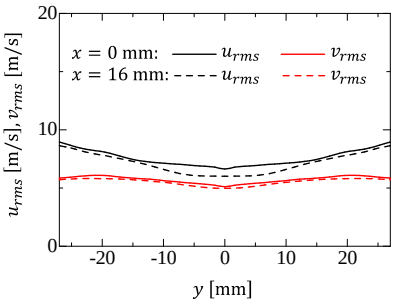

Fig. 9 Vertical profiles of rms velocity fluctuations at $x = 0$ mm and 16 mm on the midplane.

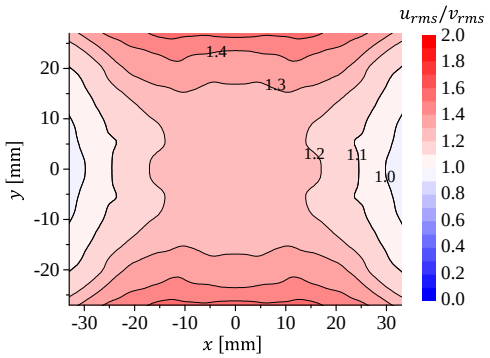

Fig. 10 The ratio of rms velocity fluctuations in the x and y directions on the midplane.

strong collision between the opposed jets rarely occurs in the present turbulence chamber. Therefore, u_{rms}/v_{rms} is slightly larger than 1 for the opposed synthetic jets.

The effects of the initial piston positions can be examined by comparing the results of two independent experiments, in each of which 300 snapshots of velocity vectors are acquired. Figure 11 shows the vertical profiles of mean velocity and rms velocity fluctuations at $x = 17$ mm of the jet plane, where the mean flow by the jet ejection is found in Fig. 7(a). Both mean velocity and rms velocity fluctuations hardly differ in the two experiments. Here, small differences can be explained by the statistical uncertainty. Therefore, the initial piston positions (phases) do not have significant influences on the statistics.

Figure 12 shows the probability density function (PDF) of u'/u_{rms} and v'/v_{rms}, which is compared with a Gaussian function. Deviation from the Gaussian function is significant for u' at $(x, y) = (0\text{ mm}, 16\text{ mm})$ of the jet plane. The shape of the PDF suggests that the flatness of u' at this location is larger than the Gaussian value 3. This is due to the strongly intermittent formation of the supersonic jets. The PDF at other locations also slightly differs from the Gaussian function. Velocity fluctuations are dominated by large-scale turbulent motions. The non-Gaussian PDF indicates that the large-scale turbulent motions even near the chamber center are influenced by the intermittency of the jet formation. Figure 13 shows the PDF of instantaneous velocity, u and v, at $(x, y) = (16\text{ mm}, 16\text{ mm})$ on the jet plane. This location is strongly influenced by the jet in the $-x$ direction. Therefore, the PDF of u' is negatively skewed. The velocity in the $-x$ direction can exceed 100 m/s even if the probability for such a large velocity is not large.

The statistical properties of turbulence generated by the opposed supersonic synthetic jets are summarized in Tab. 1. L_u and L_v are the integral length scales calculated with the longitudinal velocity auto-correlation functions f_u

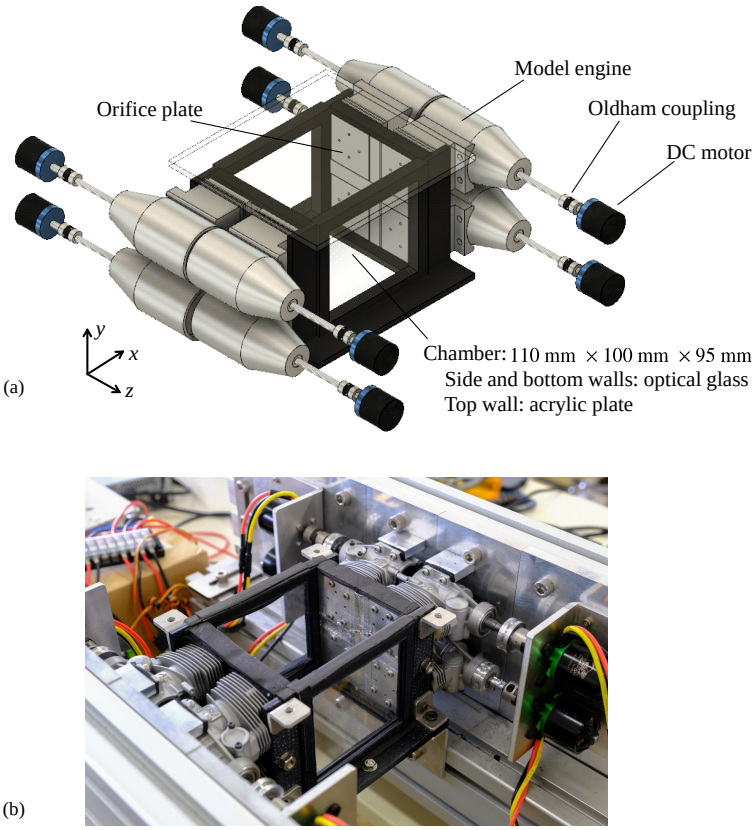

Fig. 11 Vertical profiles of (a) mean velocity and (b) rms velocity fluctuations at $x = 17$ mm of the jet plane in two independent experiments.

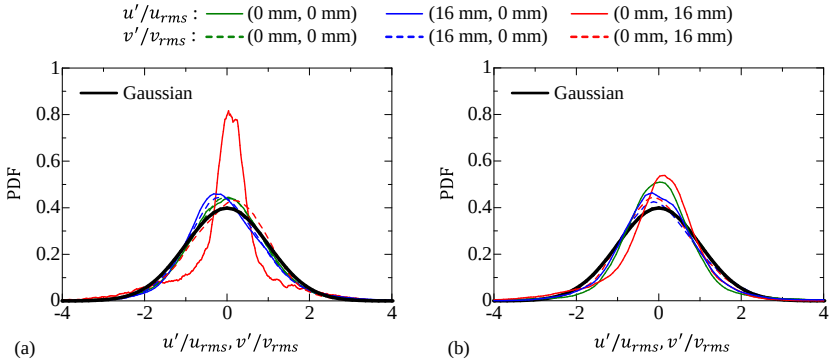

Fig. 12 Probability density functions of velocity fluctuations u'/u_{rms} and v'/v_{rms}: (a) jet plane; (b) midplane.

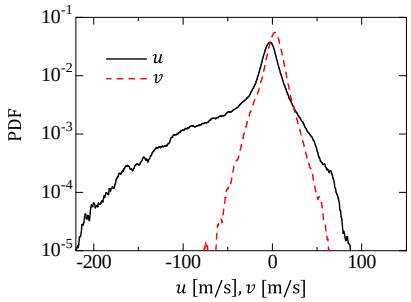

Fig. 13 Probability density functions of velocity components u and v at $(x, y) = (16\ \text{mm}, 16\ \text{mm})$ on the jet plane.

and f_v, which are defined as

$$f_u(r_x, x, y) = \overline{u'(x, y)u'(x + r_x, y)}/u^2_{rms}(x, y), \tag{3}$$

$$f_v(r_y, x, y) = \overline{v'(x, y)v'(x, y + r_y)}/v^2_{rms}(x, y). \tag{4}$$

Here, r_i is the separation distance between two points in the i direction. We evaluate f_u and f_v at $(x, y) = (0, 0)$ and drop (x, y) from the notations, i.e., $f_u(r_x)$ and $f_v(r_y)$. The integral scales of u and v are evaluated as

$$L_u = \int_0^{r_{x0}} f_u(r_x)dr_x, \quad L_v = \int_0^{r_{y0}} f_v(r_y)dr_y, \tag{5}$$

where r_{i0} is the first zero-crossing point of the auto-correlation function on the r_i axis. The Kolmogorov scale η is calculated as $\eta = (\nu^3/\varepsilon_u)^{1/4}$, where ε_u is the dissipation rate of turbulent kinetic energy and is estimated from $(\partial u/\partial x)_{rms}$ by assuming isotropy as $\varepsilon_u = 15\nu(\partial u/\partial x)^2_{rms}$ with $(\partial u/\partial x)_{rms} = \sqrt{\overline{(\partial u'/\partial x)^2}}$. Here, we use the kinematic viscosity ν at 350 K and atmospheric pressure. The turbulent Reynolds number is $Re_\lambda = u_{rms}\lambda_u/\nu$, where the Taylor microscale is defined as $\lambda_x = u_{rms}/(\partial u/\partial x)_{rms}$. The turbulent Mach number is $M_T = \sqrt{3}u_{rms}/a$, where a is the speed of sound of air at 350 K.

The integral scales in Tab. 1 are comparable for the x and y directions on both jet plane and midplane. Figure 7(c) indicates that a region with a small mean velocity (shown with white) has an approximately circular shape with a diameter of 30 mm, which is larger than the integral length scale $L_u \approx L_v \approx$ 16 mm. Therefore, the spatial variation of mean velocity occurs over a distance larger than the integral scale, and it can be expected that the effects of mean velocity gradients on turbulence are locally small at the chamber center. The integral scale on the jet plane is about 10 mm, which is smaller than 16 mm on the midplane. The length scale of large-scale turbulent motions on the jet plane can be confined by the intermittent jets at $|y| \approx 16$ mm. Consistently, the region of small mean velocity is narrower on the jet plane than on the midplane in Fig. 7. This confinement effect by the jets may explain the small L_u and L_v on the jet plane.

Table 1 Summary of turbulence statistics at the center of the jet plane ($z = 16$ mm) and the midplane ($z = 0$ mm).

	Jet plane	Midplane
$\overline{u}$ (m/s)	0.13	0.02
$\overline{v}$ (m/s)	-0.02	0.08
u_{rms} (m/s)	10.2	6.7
v_{rms} (m/s)	10.6	5.2
$\overline{u}/u_{rms}$	1.3×10^{-2}	3.0×10^{-3}
$\overline{v}/v_{rms}$	-1.9×10^{-3}	1.5×10^{-2}
Skewness (u)	6.5×10^{-2}	8.8×10^{-3}
Skewness (v)	5.6×10^{-3}	-7.3×10^{-2}
Flatness (u)	5.1	3.4
Flatness (v)	9.4	5.2
L_u (mm)	10.4	16.5
L_v (mm)	11.2	16.9
η (mm)	0.039	0.072
Re_λ	1.4×10^3	2.1×10^3
M_T	4.7×10^{-2}	3.1×10^{-2}

The center of both planes have small mean velocity compared with rms velocity fluctuations, and $\overline{u}/u_{rms}$ and $\overline{v}/v_{rms}$ are of the order of 10^{-3}-10^{-2}. Although the skewness of velocity fluctuations is close to 0, the flatness is larger than the Gaussian value of 3. The flatness larger than 3 is often interpreted as intermittency in large-scale turbulent motions (Veeravalli and Warhaft, 1989). Therefore, velocity fluctuations at the chamber center are still affected by the intermittent behaviors of the synthetic jets even though the mean velocity is close to zero.

Both planes have the Kolmogorov scale of $\eta = \mathcal{O}(10^{-2}$ mm). The spatial resolution of the PIV is $\Delta \approx 18\eta$ on the jet plane and $\Delta \approx 11\eta$ on the midplane. Thus, the spatial resolution is not sufficiently high to resolve the smallest scale of turbulence. The statistics defined with velocity gradient are not accurately evaluated with the PIV measurement. However, most length scales are resolved in the PIV with the resolution of 10η-20η. Therefore, the results are still useful for estimation of the order of derivative statistics as also confirmed in the appendix, where a direct numerical simulation database is used to assess the effect of spatial resolution on u_{rms}^2, Re_λ, and η.

The turbulent Reynolds number Re_λ reaches $\mathcal{O}(10^3)$, and a higher Re_λ can be achieved with the opposed piston-driven synthetic jets than conventional turbulence facilities used in laboratories. The turbulent Mach number is $\mathcal{O}(10^{-2})$ and the effects of compressibility are locally small at the center of the measurement planes. However, the production process of turbulence is influenced by compressibility since the jet velocity is supersonic.

The velocity statistics in the present experiment are compared with previous studies on incompressible turbulence. Figure 14 plots the longitudinal auto-correlation functions with the separation distance normalized by the integral scale. The present results are compared with the longitudinal auto-correlation function of streamwise velocity in grid turbulence (Watanabe and

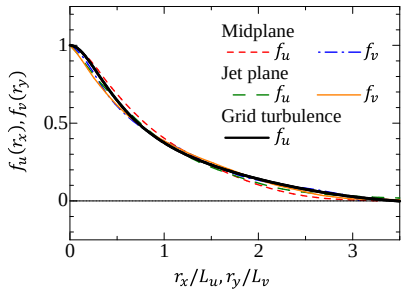

Fig. 14 Longitudinal velocity auto-correlation functions $f_u(r_x)$ and $f_v(r_y)$ at $(x, y) = (0, 0)$ on the jet plane and midplane. Figure also presents $f_u(r_x)$ in fully developed grid turbulence at $Re_\lambda = 38$ (the mesh Reynolds number defined with the mean velocity U_0 and the mesh size M is $Re_M = U_0 M/\nu = 20000$) in Watanabe and Nagata (2018).

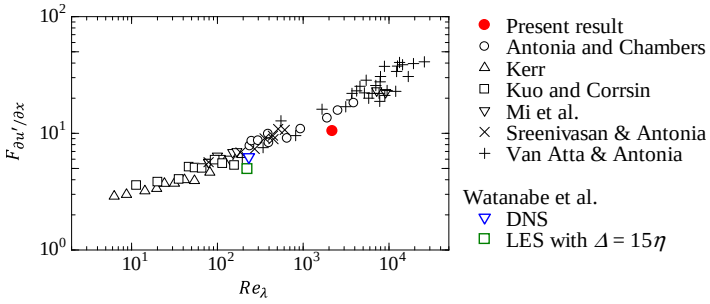

Fig. 15 Flatness of velocity derivative $\partial u'/\partial x$, $F_{\partial u'/\partial x}$, plotted as a function of turbulent Reynolds number Re_λ. The result in the present experiment is taken at the chamber center, $(x, y) = (0, 0)$ on the midplane. Figure includes the results by Antonia and Chambers (1980), Kerr (1985), Kuo and Corrsin (1971) Mi et al. (2013), Sreenivasan and Antonia (1997), and Van Atta and Antonia (1980). Some of these results were compiled by Sreenivasan and Antonia (1997). Furthermore, DNS and LES results of a turbulent planar jet in Watanabe et al. (2019) are also shown for evaluation of the effect of spatial resolution, where the LES was conducted with the cutoff length Δ close to 15 times the Kolmogorov scale η.

Nagata, 2018). f_u and f_v show a good agreement between the grid turbulence and turbulence generated by the opposed synthetic jets.

Figure 15 presents the flatness of $\partial u'/\partial x$, $F_{\partial u'/\partial x} = \overline{(\partial u'/\partial x)^4}/\overline{(\partial u'/\partial x)^2}^2$, as a function of Re_λ at the chamber center. The present result is compared with previous studies on various turbulent flows. In incompressible turbulence, the relation between $F_{\partial u'/\partial x}$ and Re_λ hardly depends on flows. The present result agrees with the trend of previous studies although the velocity field is slightly under-resolved in the PIV. We assess the resolution effect by comparing direct numerical simulation (DNS) and large eddy simulation (LES) of a turbulent planar jet (Watanabe et al., 2019), where the cutoff length of the LES is about 15η, which is estimated from velocity spectra. The flatness of the DNS and LES is also shown in Fig. 15. The LES slightly underestimate the flatness by a factor of 1.3 compared with DNS while Re_λ hardly differs between the DNS

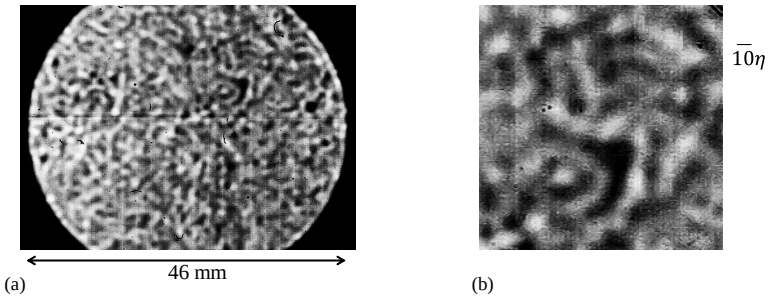

Fig. 16 (a) Shadowgraph visualization of turbulence generated by opposed piston-driven synthetic jets. (b) Close-up of (a). The length corresponding to 10η is depicted in (b), where η is taken at the chamber center.

and LES. Consistently, the present PIV yields slightly small $F_{\partial u'/\partial x}$ compared with previous studies with comparable Re_λ. Here, $F_{\partial u'/\partial x}$ of Antonia and Chambers (1980) is 1.3 times larger than the present result for comparable Re_λ. Thus, Fig. 15 implies that the relation between $F_{\partial u'/\partial x}$ and Re_λ in the turbulence generated by the opposed supersonic synthetic jets follows the quasi-universal relation observed in previous studies on turbulence although the turbulence in the present facility is generated under the strong influence of compressibility.

4.3 Shadowgraph visualization

Figure 16 shows a shadowgraph image of turbulence generated by the opposed supersonic synthetic jets. The turbulence has density variations, where there are no imprints of the jets issued from the orifice. Slightly higher brightness on the left side of the image is due to the non-uniform light intensity of the parallel light arising from the optical setup. The visualized region with a circular shape is determined by the size of the lens. The edge of the lens has a larger aberration. Therefore, the right and left edges of the visualized region may not accurately represent the density variations in turbulence.

Figure 16(b) is a close-up image of (a). The length corresponding to 10η is depicted in the figure. The characteristic length scale of brightness patterns is close to 10η. The shadowgraph image does not provide local information because the brightness is related to the density gradient integrated along the light path. Therefore, it is difficult to directly relate the shadowgraph image to the local turbulent flow field. The length 10η is close to the diameter of small-scale vortex tubes and the thickness of small-scale vortex sheet (shear layers) in turbulence (Jimenez and Wray, 1998; Watanabe et al., 2020). Therefore, one of the possible interpretations is that the brightness distribution in the shadowgraph image is related to the density gradient associated with these small-scale turbulent structures. For example, pressure p is locally small in-

side the small-scale vortex tubes, where $\nabla^2 p$ is positive. The vortex tubes are expected to have positive density Laplacian $\nabla^2 \rho > 0$ because of the correlation between pressure and density. The brightness in shadowgraph images is related to $\nabla^2 \rho$, and the bright region corresponds to $\nabla^2 \rho > 0$. Therefore, one may consider that the shapes of bright regions in Fig. 17(b) are related to small-scale vortex tubes with an approximate diameter of 10η. However, whether or not this interpretation is correct has to be examined in future studies possibly with the DNS database of compressible turbulence because the relation between the shadowgraph image to local turbulent structures is not clear.

4.4 Confinement effects by a finite chamber size

(1-3) The sidelength of the chamber is $L = 100$ mm, which yields $L/L_u \approx 6$ for the integral scale L_u at the chamber center. Small L/L_u may result in the confinement effects on turbulence. In wind tunnel experiments of grid turbulence, the tunnel confinement affects the decay of turbulence when the height and width (L_W) of the wind tunnel is not sufficiently large compared with L_u. It is widely believed that $L_W/L_u \gtrsim 10$ is sufficiently large to prevent the wind-tunnel confinement although the lowest value of L_W/L_u that is acceptable to generate freely decaying grid turbulence is not well known so far. Experiments of active-grid turbulence are often conducted with smaller L_W/L_u because active grids tend to produce turbulence with larger L_u than passive grids with the same mesh size. For example, wind-tunnel experiments of active-grid turbulence with $L_W/L_u \approx$ 3-4 are reported in Mydlarski and Warhaft (1996) and Kang et al. (2003). Despite the small values of L_W/L_u, the decay properties in their experiments are in agreement with other experiments of grid turbulence as also discussed in Djenidi et al. (2015). Similar issues of the domain size are also known in numerical simulations of decaying isotropic turbulence in a triply periodic domain. Anas et al. (2020) reported that the decay exponent of turbulent kinetic energy is influenced by the domain size L_S when L_S is smaller than about $3.3L_u$. The ratio $L/L_u = 6.3$ in the present experiment is larger than these values in active-grid turbulence ($L_W/L_u \approx$ 3-4) and DNS of decaying isotropic turbulence ($L_S/L_u = 3.3$).

The above examples of grid turbulence and isotropic turbulence in a periodic box concern the decay of turbulence. The confinement effects may depend on flow configurations. In the present apparatus, statistically steady turbulence is generated in the closed chamber. The jets ejected from the orifices interact with the chamber sidewall. The minimum distance between the orifice and the wall is $D_W = 21.5$ mm, which is about 10 times the orifice diameter $d = 2$ mm. Studies on an offset jet over a wall indicate that the jet formation is influenced by the wall for $D_W/d \approx 10$ (Assoudi et al., 2019). From these studies on the offset jet, it is expected that the outmost jets in the present experiment are inclined toward the wall and the recirculation zones are formed between the jets and the wall. However, each synthetic jet actuator used in this study

generates four jets, which also interact with each other. It is known that two parallel jets have similar features to the offset jet: the parallel jets also generate a recirculation zone between the jets and the jet axes are tilted toward the other jet (Nasr and Lai, 1997). Therefore, the interaction among the jets in the present apparatus may cause an opposite effect from the wall influence: the outmost jets can be inclined toward the chamber center due to the interaction with the adjacent jets. The measurement area of the PIV covers the innermost jets on the jet plane. At least, the jet axes found in the mean velocity field (Fig. 7) are almost parallel to the x axis, and the wall influences seem to be negligible to the innermost jets.

4.5 Possible influences of the intermittent jet formation on turbulence characteristics

(1-1) The jet formation of the piston-driven synthetic jet actuators is more intermittent than that of conventional synthetic jet actuators (Crittenden and Glezer, 2006; Sakakibara et al., 2018). It is reasonable to interpret the jet formation as the energy input to turbulence. The jets are ejected from each actuator at the frequency of $f = 150$ Hz. Because the eight actuators are operated without matching the phases, the mean interval between the jet ejections is roughly estimated as $T_{in} = (8f)^{-1} \approx 8.3 \times 10^{-4}$ (s). The time scale of large-scale turbulent motions is $T_0 = L_u/u_{rms} \approx 2.5 \times 10^{-3}$ (s) at the chamber center. Thus, the energy injection has a shorter time scale than the large-scale turbulent motions.

For $T_{in} \gg T_0$, the turbulence in the chamber decays after the jets are ejected from one actuator, and then the turbulence is amplified again by the next jet ejection from another actuator. In this case, the statistical properties of turbulence also temporally oscillate because of the intermittent energy input by the jet formation. Then, the statistics should be defined as functions of time, for which time averages are not adequate. A DNS study confirmed that isotropic turbulence subjected to temporally-oscillating external forcing has a significant spectral imbalance between the energy cascade from large to small scales and the energy dissipation that occurs at small scales (Valente et al., 2014). This imbalance leads to the non-equilibrium behavior of the turbulent kinetic energy dissipation rate. However, this situation is unlikely in the present experiment because of $T_{in} < T_0$.

The opposite situation $T_{in} \ll T_0$ indicates the nearly continuous energy input to turbulence, where the time scale of energy-input fluctuations, T_{in}, is small. This situation can be realized in DNS of statistically-steady isotropic turbulence with a random force (Alvelius, 1999), for which a classical equilibrium relation between the energy cascade and the dissipation holds. The turbulence generated in the present experiment possesses $T_{in}/T_0 = 0.3$, which satisfies $T_{in} < T_0$ although the ratio is not small enough to assume $T_{in} \ll T_0$. After the jet ejection from one actuator, the turbulence in the chamber is expected to decay until another jet ejection, where the mean interval between the

jet ejections is $0.3T_0$. Previous DNS studies suggest that the decay over $0.3T_0$ is not significant as explained below. A similar decay process of turbulence can be mimicked by the DNS of isotropic turbulence. At first, DNS is performed with an external forcing to generate statistically steady isotropic turbulence. Subsequently, the forcing is switched off to allow the decay of turbulence. It was shown in such DNS that temporal variations of turbulence statistics due to the decay are very small over $0.3T_0$, for which the change is less than 10% of the initial values for turbulent kinetic energy and its dissipation rate (Valente et al., 2014; Yoffe and McComb, 2018). In this case, time averages are still useful to evaluate the statistical properties of turbulence. It should be noted that phase-locked averages are necessary to investigate the formation of each synthetic jet although the present study concerns the turbulence near the chamber center. These considerations imply that the turbulence dynamics, such as the behavior of the energy cascade and the dissipation rate, is not significantly altered by the intermittency of the synthetic jet formation.

4.6 Comparisons with other methods of generating nearly isotropic turbulence

(1-1) The PIV measurement confirms that nearly isotropic turbulence is generated at the chamber center. Since the interaction among supersonic jets occurs in the chamber, turbulence is generated under the influence of compressibility. Experiments of incompressible isotropic turbulence have widely been conducted with turbulence-generating grids installed in subsonic wind tunnels (Uberoi and Wallis, 1967). Experiments of compressible grid turbulence have been conducted with shock-tube facilities or transonic/supersonic wind tunnels, in which a high-speed flow passes a grid (Keller and Merzkirch, 1990). As discussed in the introduction, shock tubes are often used to investigate the interaction between shock waves and turbulence. The shock tubes and most of the high-speed wind tunnels are short-duration facilities, which produce a steady flow that lasts for a very short time period. The duration time can be shorter than 1 s (Wu and Radespiel, 2017). In the case of blowdown supersonic wind tunnels, how long the steady flow lasts depends on the air supply system (e.g., the volume of a tank and the pressure of gas) and the cross-sectional size of the test section. Therefore, some supersonic wind tunnels have a narrow and small test section to achieve a steady flow over a longer time (Bharath, 2015). For example, grid turbulence was generated in a supersonic wind tunnel whose test section has a 12 mm $\times$ 10 mm cross section (Kouchi et al., 2020). Small test sections are not suited for grid turbulence because the mesh size of the grid also has to be small to prevent the wind tunnel confinement and a higher spatial resolution is required for measurements. Statistical analyses are important to investigate turbulent flows. However, short-duration facilities have difficulty in dealing with the accurate evaluation of turbulence statistics with time averages. In addition to time averages, ensemble averages are necessary for the evaluation of statistics although

repeating experiments with supersonic wind tunnels can be time-consuming because it takes time to prepare for the wind tunnel operation, e.g., supplying pressurized air in a storage tank.

The present apparatus uses the piston-driven synthetic jet actuators, which do not rely on pressurized air stored in external tanks because the air in the chamber is taken into the cylinder by the piston and is ejected as a high-speed jet. This feature allows the continuous operation of the apparatus to realize statistically steady turbulence. Therefore, it is easy to conduct measurements over a long time interval for the accurate evaluation of statistics. In addition, the opposed supersonic synthetic jets can generate turbulence with a much smaller mean velocity than grid turbulence in supersonic wind tunnels. For a similar level of turbulent Mach number, the instantaneous velocity is much larger in grid turbulence with a mean flow. Therefore, the velocity measurement (especially with PIV) is relatively easier for turbulence with a small mean velocity since the instantaneous velocity of grid turbulence in supersonic wind tunnels can be much larger than 100 m/s. Turbulence chambers with a small mean velocity are often developed with electrical fans or conventional synthetic jet actuators, which only generate subsonic flows (Ravi et al., 2013; Hwang and Eaton, 2004). The basic idea of this study is the same as those previous experiments. However, the piston-driven synthetic jet actuators extend the velocity range to the compressible regime since it is capable of generating a supersonic flow.

One of the important parameters in compressible turbulence is the turbulent Mach number M_T. DNS and experiments of incompressible turbulence have observed that the velocity derivative skewness and flatness have universal relations with Re_λ (Sreenivasan and Antonia, 1997). Strong compressibility effects result in deviations from these universal relations obtained for incompressible turbulence (Watanabe et al., 2021). However, DNS of compressible isotropic turbulence showed that the deviations from incompressible values are not characterized solely by M_T, indicating that M_T is not a single parameter that determines the compressibility effects on turbulence (Donzis and John, 2020). The compressibility effects in DNS of forced compressible turbulence differ significantly between solenoidal forcing schemes and mixed dilatational/solenoidal forcing schemes (Donzis and John, 2020). Therefore, the compressibility effects on turbulence depend on the turbulence generation process. It is important to conduct experiments of compressible turbulence with various facilities and turbulent generators. In this sense, the turbulence chamber developed with the piston-driven synthetic jet actuators can provide unique data of compressible turbulence.

5 Conclusions

We have experimentally investigated the turbulence generated by an array of the opposed piston-driven synthetic jet actuators, each of which consists of a piston/cylinder actuator connected to a DC motor and an orifice plate on

the cylinder top. The interaction among 32 supersonic synthetic jets generates turbulence in a closed chamber. Once the actuators are turned on, the temperature in the chamber rises to about 350 K, which hardly varies with time. Large temperature variations in the cylinder generate oil mist, which can be used as the tracer particles of PIV measurement. The turbulence with small mean velocity forms at the chamber center, where the rms velocity fluctuations are also almost uniform in space. The rms velocity fluctuations at the chamber center are about 1.2 times larger in the jet direction than in other directions. Although the mean velocity is negligible at the chamber center, large-scale velocity fluctuations are intermittent as confirmed from the flatness of velocity fluctuations greater than 3. The shape of the auto-correlation function agrees well with grid turbulence. The relation between the velocity derivative flatness and turbulent Reynolds number also follows the trend observed in previous studies on turbulence. The turbulent Reynolds number reaches $O(10^3)$ and the turbulent Mach number is $O(10^{-2})$ at the chamber center, where the compressibility effects may be locally weak. However, the instantaneous velocity of the synthetic jets exceeds 100 m/s. The generation process of turbulence due to the supersonic jet is strongly influenced by compressibility effects. A shadowgraph image visualizes density variations, where the brightness distribution in the image has a characteristic length related to the Kolmogorov scale. The present experiment was conducted with simple orifice holes. However, usage of the jet nozzle with different geometries, such as a divergent-convergent nozzle, may modify the characteristics of generated turbulence, such as jet Mach numbers of supersonic synthetic jets, turbulent Mach number, and turbulent Reynolds number. This feature makes the present facility useful for future investigation of turbulence under a wide range of compressibility effects.

Acknowledgements The authors acknowledge Mr. H. Sakakibara for his help in developing the piston-driven synthetic jet actuators. This work was supported by JSPS KAKENHI Grant Number 18H01367, Paloma Environmental Technology Development Foundation, and Tatematsu Foundation.

Conflict of interest

The authors declare that they have no conflict of interest.

Appendix: Effects of spatial resolution

The PIV measurement conducted in this study has a spatial resolution of 10η-20η. The effects of the unresolved velocity fluctuations on velocity statistics are assessed with direct numerical simulation (DNS) of turbulence. Here, we use the DNS database of a temporally-evolving turbulent planar jet with the jet Reynolds number of 40000 (Watanabe et al., 2019). An energy spectrum of streamwise velocity fluctuations $E_u(k_x)$ is calculated on the jet centerline, where k_x is the streamwise wavenumber. We define the cutoff wavenumber as

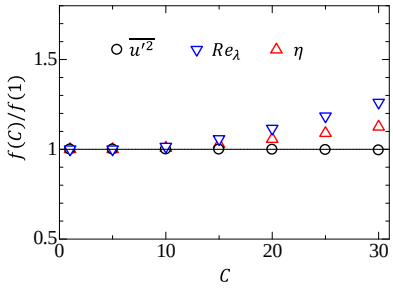

Fig. 17 Effects of the spatial resolution on velocity variance $\overline{u'^2}(C)$, turbulent Reynolds number $Re_\lambda(C)$, and Kolmogorov scale $\eta(C)$, which are defined for filtered velocity with a cutoff length scale of $C\eta_0$. $f = \overline{u'^2}(C)$, $Re_\lambda(C)$, and $\eta(C)$ are normalized by $f(C = 1)$.

$k_C = 2\pi/C\eta_0$ with a parameter C and the Kolmogorov scale η_0. Here, η_0 is calculated with the turbulent kinetic energy dissipation rate $\varepsilon = 2\nu\overline{S_{ij}S_{ij}}$, where S_{ij} is the rate-of-strain tensor. Streamwise velocity variance contributed from the scales greater than $C\eta_0$ is evaluated as $\overline{u'^2}(C) = \int_0^{k_C} E_u(k_x)dk_x$. Similarly, the variance of $\partial u/\partial x$ at scales greater than $C\eta_0$ is given by $\overline{(\partial u'/\partial x)^2}(C) = \int_0^{k_C} k_x^2 E_u(k_x)dk_x$. Then, the turbulent Reynolds number $Re_\lambda(C)$ and Kolmogorov scale $\eta(C)$ of the filtered velocity are calculated with $\overline{u'^2}(C)$ and $\overline{(\partial u'/\partial x)^2}(C)$:

$$Re_\lambda(C) = \frac{\overline{u'^2}}{\nu\sqrt{\overline{(\partial u'/\partial x)^2}}}, \quad \eta(C) = \left(\frac{\nu^2}{15\overline{(\partial u'/\partial x)^2}}\right)^{1/4}. \tag{6}$$

Figure 17 shows the cutoff-length dependence of $\overline{u'^2}(C)$, $Re_\lambda(C)$, and $\eta(C)$ normalized by their values for $C = 1$. As C increases, the range of the unresolved scale becomes wider. Because velocity fluctuations are dominated by large-scale turbulent motions, $\overline{u'^2}(C)/\overline{u'^2}(1)$ stays 1 even for $C = 30$. $Re_\lambda(C)$ and $\eta(C)$ increase with C. However, $Re_\lambda(C)/Re_\lambda(1)$ and $\eta(C)/\eta(1)$ are less than 1.3 even at $C = 30$. Thus, the present PIV measurement with the spatial resolution of 10η-20η is still useful for the approximate estimation of turbulent Reynolds number and Kolmogorov scale.

References

Agui JH, Briassulis G, Andreopoulos Y (2005) Studies of interactions of a propagating shock wave with decaying grid turbulence: velocity and vorticity fields. J Fluid Mech 524:143–195

Alvelius K (1999) Random forcing of three-dimensional homogeneous turbulence. Phys Fluids 11(7):1880–1889

Anas M, Joshi P, Verma MK (2020) Freely decaying turbulence in a finite domain at finite Reynolds number. Phys Fluids 32(9):095109

Antonia RA, Chambers AJ (1980) On the correlation between turbulent velocity and temperature derivatives in the atmospheric surface layer. Boundary-Layer Meteorol 18(4):399–410

Assoudi A, Saïd NM, Bournot H, Le Palec G (2019) Comparative study of flow characteristics of a single offset jet and a turbulent dual jet. Heat Mass Transf 55(4):1109–1131

Bellani G, Variano EA (2014) Homogeneity and isotropy in a laboratory turbulent flow. Exp Fluids 55(1):1–12

Beresh S, Kearney S, Wagner J, Guildenbecher D, Henfling J, Spillers R, Pruett B, Jiang N, Slipchenko M, Mance J, S R (2015) Pulse-burst PIV in a high-speed wind tunnel. Meas Sci Tech 26(9):095305

Bharath BK (2015) Design and fabrication of a supersonic wind tunnel. Int J Eng Appl Sci 2(5):257914

Birouk M, Sarh B, Gökalp I (2003) An attempt to realize experimental isotropic turbulence at low Reynolds number. Flow, Turbul Combust 70(1-4):325–348

Bonnet JP, Jayaraman V, De Roquefort TA (1984) Structure of a high-Reynolds-number turbulent wake in supersonic flow. J Fluid Mech 143:277–304

Bradley D, Lawes M, Morsy ME (2019) Measurement of turbulence characteristics in a large scale fan-stirred spherical vessel. J Turbul 20(3):195–213

Briassulis G, Agui JH, Andreopoulos Y (2001) The structure of weakly compressible grid-generated turbulence. J Fluid Mech 432:219–283

Carter D, Petersen A, Amili O, Coletti F (2016) Generating and controlling homogeneous air turbulence using random jet arrays. Exp Fluids 57(12):1–15

Clemens NT, Mungal MG (1995) Large-scale structure and entrainment in the supersonic mixing layer. J Fluid Mech 284:171–216

Comte-Bellot G, Corrsin S (1966) The use of a contraction to improve the isotropy of grid-generated turbulence. J Fluid Mech 25(4):657–682

Crittenden TM, Glezer A (2006) A high-speed, compressible synthetic jet. Phys Fluids 18(1):017107

Davidson PA (2004) Turbulence: An Introduction for Scientists and Engineers. Oxford Univ. Pr.

De Silva IPD, Fernando HJS (1994) Oscillating grids as a source of nearly isotropic turbulence. Phys Fluids 6(7):2455–2464

Djenidi L, Kamruzzaman M, Antonia RA (2015) Power-law exponent in the transition period of decay in grid turbulence. J Fluid Mech 779:544–555

Donzis DA, John JP (2020) Universality and scaling in homogeneous compressible turbulence. Phys Rev Fluids 5(8):084609

Fincham AM, Maxworthy T, Spedding GR (1996) Energy dissipation and vortex structure in freely decaying, stratified grid turbulence. Dyn Atmos Oceans 23(1-4):155–169

Gilarranz JL, Traub LW, Rediniotis OK (2005) A new class of synthetic jet actuators–Part I: design, fabrication and bench top characterization. ASME J Fluids Eng 127(2):367–376

Goepfert C, Marié JL, Chareyron D, Lance M (2010) Characterization of a system generating a homogeneous isotropic turbulence field by free synthetic jets. Exp Fluids 48(5):809–822

Honkan A, Andreopoulos J (1992) Rapid compression of grid-generated turbulence by a moving shock wave. Phys Fluids 4(11):2562–2572

Hopfinger EJ, Toly JA (1976) Spatially decaying turbulence and its relation to mixing across density interfaces. J Fluid Mech 78(1):155–175

Hwang W, Eaton JK (2004) Creating homogeneous and isotropic turbulence without a mean flow. Exp Fluids 36(3):444–454

Hwang W, Eaton JK (2006) Homogeneous and isotropic turbulence modulation by small heavy ($St \sim 50$) particles. J Fluid Mech 564:361

Jimenez J, Wray AA (1998) On the characteristics of vortex filaments in isotropic turbulence. J Fluid Mech 373:255–285

Kang HS, Chester S, Meneveau C (2003) Decaying turbulence in an active-grid-generated flow and comparisons with large-eddy simulation. J Fluid Mech 480:129–160

Keller J, Merzkirch W (1990) Interaction of a normal shock wave with a compressible turbulent flow. Exp Fluids 8(5):241–248

Kerr RM (1985) Higher-order derivative correlations and the alignment of small-scale structures in isotropic numerical turbulence. J Fluid Mech 153:31–58

Kitamura T, Nagata K, Sakai Y, Sasoh A, Terashima O, Saito H, Harasaki T (2014) On invariants in grid turbulence at moderate Reynolds numbers. J Fluid Mech 738:378–406

Klewicki JC, Hirschi CR (2004) Flow field properties local to near-wall shear layers in a low Reynolds number turbulent boundary layer. Phys Fluids 16(11):4163–4176

Kouchi T, Iwachido M, Nakagawa T, Nagata Y, Yanase S (2020) Transverse jet mixing in a supersonic grid turbulence. In: Proceedings of the AIAA Scitech 2020 Conference, p 2040

Kovasznay LSG (1950) The hot-wire anemometer in supersonic flow. J Aero Sciences 17(9):565–572

Krawczynski JF, Renou B, Danaila L (2010) The structure of the velocity field in a confined flow driven by an array of opposed jets. Phys Fluids 22(4):045104

Krogstad PÅ, Davidson PA (2010) Is grid turbulence saffman turbulence? J Fluid Mech 642:373

Kuo AYS, Corrsin S (1971) Experiments on internal intermittency and fine-structure distribution functions in fully turbulent fluid. J Fluid Mech 50(2):285–319

Marié JL, Tronchin T, Grosjean N, Méès L, Öztürk OC, Fournier C, Barbier B, Lance M (2017) Digital holographic measurement of the Lagrangian evaporation rate of droplets dispersing in a homogeneous isotropic turbulence.

Exp Fluids 58(2):11
Mi J, Xu M, Zhou T (2013) Reynolds number influence on statistical behaviors of turbulence in a circular free jet. Phys Fluids 25(7):075101
Mydlarski L, Warhaft Z (1996) On the onset of high-Reynolds-number grid-generated wind tunnel turbulence. J Fluid Mech 320(1):331–368
Nasr A, Lai J (1997) Comparison of flow characteristics in the near field of two parallel plane jets and an offset plane jet. Phys Fluids 9(10):2919–2931
Ozono S, Ikeda H (2018) Realization of both high-intensity and large-scale turbulence using a multi-fan wind tunnel. Exp Fluids 59(12):1–12
Pérez-Alvarado A, Mydlarski L, Gaskin S (2016) Effect of the driving algorithm on the turbulence generated by a random jet array. Exp Fluids 57(2):20
Praud O, Fincham AM, Sommeria J (2005) Decaying grid turbulence in a strongly stratified fluid. J Fluid Mech 522:1–33
Ravi S, Peltier SJ, Petersen EL (2013) Analysis of the impact of impeller geometry on the turbulent statistics inside a fan-stirred, cylindrical flame speed vessel using piv. Exp Fluids 54(1):1424
Sakakibara H, Watanabe T, Nagata K (2018) Supersonic piston synthetic jets with single/multiple orifice. Exp Fluids 59(5):76
Scarano F, Van Oudheusden BW (2003) Planar velocity measurements of a two-dimensional compressible wake. Exp Fluids 34(3):430–441
Semenov ES (1965) Measurement of turbulence characteristics in a closed volume with artificial turbulence. Combust Explos ShockWaves 1(2):57–62
Sreenivasan KR, Antonia RA (1997) The phenomenology of small-scale turbulence. Annu Rev Fluid Mech 29(1):435–472
Takamure K, Ozono S (2019) Relative importance of initial conditions on outflows from multiple fans. Phys Rev E 99(1):013112
Tamba T, Fukushima G, Kayumi M, Iwakawa A, Sasoh A (2019) Experimental investigation of the interaction of a weak planar shock with grid turbulence in a counter-driver shock tube. Phys Rev Fluids 4(7):073401
Thompson SM, Turner JS (1975) Mixing across an interface due to turbulence generated by an oscillating grid. J Fluid Mech 67(2):349–368
Traub LW, Sweet M, Nilssen K (2012) Evaluation and characterization of a lateral synthetic jet actuator. J Aircraft 49(4):1039–1050
Uberoi MS, Wallis S (1967) Effect of grid geometry on turbulence decay. Phys Fluids 10:1216–1224
Valente PC, Vassilicos JC (2011) The decay of turbulence generated by a class of multiscale grids. J Fluid Mech 687:300–340
Valente PC, Onishi R, da Silva CB (2014) Origin of the imbalance between energy cascade and dissipation in turbulence. Phys Rev E 90(2):023003
Van Atta CW, Antonia RA (1980) Reynolds number dependence of skewness and flatness factors of turbulent velocity derivatives. Phys Fluids 23(2):252–257
Variano EA, Cowen EA (2008) A random-jet-stirred turbulence tank. J Fluid Mech 604:1–32

Variano EA, Bodenschatz E, Cowen EA (2004) A random synthetic jet array driven turbulence tank. Exp Fluids 37(4):613–615

Veeravalli S, Warhaft Z (1989) The shearless turbulence mixing layer. J Fluid Mech 207:191–229

Watanabe T, Nagata K (2018) Integral invariants and decay of temporally developing grid turbulence. Phys Fluids 30(10):105111

Watanabe T, Zhang X, Nagata K (2019) Direct numerical simulation of incompressible turbulent boundary layers and planar jets at high Reynolds numbers initialized with implicit large eddy simulation. Comput Fluids 194:104314

Watanabe T, Tanaka K, Nagata K (2020) Characteristics of shearing motions in incompressible isotropic turbulence. Phys Rev Fluids 5(7):072601

Watanabe T, Tanaka K, Nagata K (2021) Solenoidal linear forcing for compressible, statistically steady, homogeneous isotropic turbulence with reduced turbulent mach number oscillation. Phys Fluids 33(9):095108

Wernet MP (2007) Temporally resolved PIV for space–time correlations in both cold and hot jet flows. Meas Sci Tech 18(5):1387

Wernet MP (2016) Application of Tomo-PIV in a large-scale supersonic jet flow facility. Exp Fluids 57(9):144

Williams O, Van Buren T, Smits AJ (2015) A new method for measuring turbulent heat fluxes using PIV and fast-response cold-wires. Exp Fluids 56(7):1–10

Wu J, Radespiel R (2017) Damping insert materials for settling chambers of supersonic wind tunnels. Exp Fluids 58(3):19

Xiang X, Madison TJ, Sellappan P, Spedding GR (2015) The turbulent wake of a towed grid in a stratified fluid. J Fluid Mech 775:149–177

Xu S, Huang S, Huang R, Wei W, Cheng X, Ma Y, Zhang Y (2017) Estimation of turbulence characteristics from PIV in a high-pressure fan-stirred constant volume combustion chamber. Appl Therm Eng 110:346–355

Yap CT, Van Atta CW (1993) Experimental studies of the development of quasi-two-dimensional turbulence in stably stratified fluid. Dyn Atmos Oceans 19(1-4):289–323

Yoffe SR, McComb WD (2018) Onset criteria for freely decaying isotropic turbulence. Phys Rev Fluids 3(10):104605

Zimmermann R, Xu H, Gasteuil Y, Bourgoin M, Volk R, Pinton J, Bodenschatz E (2010) The Lagrangian exploration module: An apparatus for the study of statistically homogeneous and isotropic turbulence. Rev Sci Instrum 81(5):055112

Zwart PJ, Budwig R, Tavoularis S (1997) Grid turbulence in compressible flow. Exp Fluids 23(6):520–522